

A Two Transition State Model for Radical–Molecule Reactions: A Case Study of the Addition of OH to C₂H₄

Erin E. Greenwald and Simon W. North

Department of Chemistry, Texas A&M University, P.O. Box 30012, College Station, Texas 77842

Yuri Georgievskii and Stephen J. Klippenstein*

Combustion Research Facility, Sandia National Laboratories, Livermore, California 94551-0969

Received: February 7, 2005; In Final Form: April 6, 2005

A two transition state model is applied to the study of the addition of hydroxyl radical to ethylene. This reaction serves as a prototypical example of a radical–molecule reaction with a negative activation energy in the high-pressure limit. The model incorporates variational treatments of both inner and outer transition states. The outer transition state is treated with a recently derived long-range transition state theory approach focusing on the longest-ranged term in the potential. High-level quantum chemical estimates are incorporated in a variational transition state theory treatment of the inner transition state. Anharmonic effects in the inner transition state region are explored with direct phase space integration. A two-dimensional master equation is employed in treating the pressure dependence of the addition process. An accurate treatment of the two separate transition state regions at the energy and angular momentum resolved level is essential to the prediction of the temperature dependence of the addition rate. The transition from a dominant outer transition state to a dominant inner transition state is predicted to occur at about 130 K, with significant effects from both transition states over the 10 to 400 K temperature range. Modest adjustment in the *ab initio* predicted inner saddle point energy yields theoretical predictions which are in quantitative agreement with the available experimental observations. The theoretically predicted capture rate is reproduced to within 10% by the expression $[4.93 \times 10^{-12} (T/298)^{-2.488} \exp(-107.9/RT) + 3.33 \times 10^{-12} (T/298)^{0.451} \exp(117.6/RT)]$; with $R = 1.987$ and T in K] cm³ molecules⁻¹ s⁻¹ over the 10–600 K range.

I. Introduction

Many radical–molecule reactions exhibit negative activation energies, with their rate coefficients decreasing with increasing temperature, even in the high-pressure limit. For example, negative activation energies have been noted for a wide variety of olefin reactions with Cl atoms,^{1–4} with O(³P) atoms,^{5–9} and with hydroxyl radicals.¹⁰ The role of negative activation energies has also been widely discussed in the reactions of hydrocarbon radicals with hydrogen halides and the related reverse reactions.^{11–16}

The reactions of olefins with hydroxyl radical are important in a variety of combustion and atmospheric contexts. For example, the predominant reaction in the atmosphere is electrophilic addition of OH to olefins. The addition of OH to ethylene represents the simplest example of this class of reactions and is, therefore, a benchmark system for understanding the underlying nature of these reactions. As a consequence, there have been numerous experimental^{17–53} and theoretical^{54–62} studies of this reaction.

In the range of low to moderate temperatures, the mechanism is dominated by electrophilic addition of the hydroxyl radical to ethylene. At higher temperatures, the mechanism changes as first redissociation of the stabilized adduct becomes significant at about 450 K,³⁶ and then either abstraction and/or isomerization of the adduct to ethoxy radical, followed by further reaction,

becomes significant at about 600 K.^{43,44} Most of the experimental studies have focused on the observation of the thermal rate coefficients at room temperature or higher. Near room temperature the high-pressure limit is approached at pressures of about 1 atm.^{36,37,51} The high-pressure addition rate constant for C₂H₄ + OH was generally found to decrease slightly with increasing temperature in the 100–600 K range, with measured Arrhenius activation energies ranging from –2.3 to 0.0 kcal/mol.^{23,31,36,43,51,53} Lower-temperature studies have been limited to Leone and co-workers’⁵³ study over the temperature range from 96 to 296 K using the pulsed Laval nozzle technique. Although relatively low pressures were employed in this study (e.g., less than 1 Torr for the lower temperatures), it was argued that the results still pertained to the high-pressure limit due to the increase in the lifetime of the complex with decreasing temperature. The combined experimental data over the 96–600 K range provides a stringent test for modern rate theory.

Theoretical studies of the C₂H₄ + OH reaction have considered quantum chemical analyses of the stationary points on the potential energy surface^{54–62} as well as transition state theory based analyses of the kinetics.^{56,58–60,62} The quantum chemical analyses have provided fairly detailed descriptions of the saddle point connecting the entrance van der Waals complex with the CH₂CH₂OH adduct, as well as mapping out the full reactive potential energy surface. The transition state theory analyses of the addition rate have focused on the effect of only this saddle point on the entrance channel kinetics.^{56,59} Other aspects of the kinetics, such as the abstraction kinetics and the isomerization/

* To whom correspondence should be addressed. E-mail: sjklipp@sandia.gov.

dissociation kinetics of the initial adduct, have also been considered.^{58,60,62}

The appearance of a negative activation energy in the experiments has been correlated with a negative energy of the entrance channel saddle point relative to reactants.⁵⁶ However, a negative value for the saddle point energy necessarily implies that, at least in some energy range near the reaction threshold, there is a second transition state at large separations. This “outer” transition state must provide the dominant bottleneck at low energies (or temperatures), while the “inner” transition state, located in the neighborhood of the saddle point, should provide the dominant bottleneck at higher energies (or temperatures). At intermediate temperatures, the bottlenecks in the flux through both the inner and the outer transition state will contribute to determining the overall rate and thus its temperature dependence. A proper rationalization of the negative activation energy must consider the combined effect of these two transition states.

The recent theoretical analysis of the $\text{C}_2\text{H}_4 + \text{OH}$ reaction by Vivier-Bunge and co-workers,⁵⁹ building on earlier work of Singleton and Cvetanovic,⁶³ recognized the significance of the outer transition state preceding the van der Waals complex. Implementing a steady-state assumption for the concentration of van der Waals complexes they suggested that the overall addition rate coefficient is given by

$$k = k_1 k_2 / (k_{-1} + k_2) \quad (1)$$

where k_1 and k_{-1} are the thermal rate coefficients for formation and decomposition of the van der Waals complex from reactants, while k_2 is the thermal rate coefficient for conversion of the van der Waals complex into the chemical adduct. Vivier-Bunge and co-workers then went on to derive expressions for the activation energy under the assumption that k_{-1} is much greater than k_2 and so the overall rate coefficient can be simplified to $k_1 k_2 / k_{-1}$.

There are multiple problems with this analysis. First, the assumption of $k_{-1} \gg k_2$ is not valid in precisely the interesting temperature region where the two transition states provide a comparable bottleneck to the reactive flux. An even more fundamental flaw is that the standard steady-state analysis⁶⁴ leading to eq 1 is implemented at the *canonical* level, which in effect presumes that the van der Waals complexes have a thermal distribution of states. This thermal distribution would only arise if the van der Waals complexes suffer many collisions before reacting. The shallowness of the van der Waals wells suggests that this is seldom if ever true. As a result, eq 1, with thermal rate coefficients, is essentially never applicable.

A more appropriate assumption is that the dynamics in the region of the van der Waals complex occurs in a collision-free environment with total energy, E , and total angular momentum, J , conserved.⁶⁵ The inner and outer transition states then act as a series of bottlenecks to reaction. A reasonable approximation to the effective flux through both transition states is given by

$$N_{\text{eff}}^\ddagger(E, J) = N_{\text{outer}}^\ddagger(E, J) N_{\text{inner}}^\ddagger(E, J) / (N_{\text{outer}}^\ddagger(E, J) + N_{\text{inner}}^\ddagger(E, J)) \quad (2)$$

where $N_{\text{inner}}^\ddagger$ and $N_{\text{outer}}^\ddagger$ are the E and J resolved transition state numbers of states at the inner and outer transition states, respectively. In writing eq 2, we are presuming statistical probabilities for crossing each transition state dividing surface, and further that the maximum in the flux at the van der Waals minimum greatly exceeds that at the two transition states.^{66,67} The “high pressure” addition rate constant for this effective transition state model is provided by the standard Boltzmann

average of the effective transition state flux

$$k^\infty(T) = \frac{1}{h Q_{\text{reactants}}} \int N_{\text{eff}}^\ddagger(E, J) \exp\left(-\frac{E}{k_B T}\right) dE dJ \quad (3)$$

where we are considering a pressure that yields a collision rate that is high relative to redissociation of the chemical adduct, but that is low relative to the dissociation of the van der Waals complex.

Now, in the limit where the flux through the outer bottleneck greatly exceeds that through the inner bottleneck, k^∞ reduces to k_2 , as it should. Note that the expression in eq 2 is closely related to that of eq 1, essentially involving the replacement of the canonical rate coefficients with E and J resolved rate coefficients. It corresponds to the implementation of a steady-state assumption at the E and J resolved level. This replacement will prove to be of crucial importance to the proper modeling of the temperature dependence of the $\text{C}_2\text{H}_4 + \text{OH}$ reaction and of other related reactions.

In this article, we provide a detailed application of eqs 2 and 3 to the evaluation of the high-pressure addition rate coefficient for the $\text{C}_2\text{H}_4 + \text{OH}$ reaction. To make proper comparisons with experiment we also implement eq 2 for the transition state flux within a two-dimensional (2D) (in E and J) master equation analysis of the pressure dependence. Related two transition state models for radical–molecule reactions were first considered by Benson and co-workers,⁶⁸ where they considered the effect of the transition states for an entrance and an exit channel acting in series. Subsequent studies by Rauk and co-workers⁶⁹ and by Rayez and co-workers⁷⁰ have applied this model to reactions with two separate transition states in the entrance channel, but with somewhat limited models for the outer transition state. Here, we build on these earlier works by applying more accurate, *a priori* models for both the inner and outer transition states, with a specific illustration of the $\text{C}_2\text{H}_4 + \text{OH}$ reaction. The results from this study are of both specific and general interest. Notably, this two transition state picture has already proven to be essential to the quantitative understanding of the dynamics of barrierless reactions such as $\text{NC} + \text{NO}$ ⁶⁷ and ${}^1\text{CH}_2 + \text{CO}$,⁷¹ where there is no inner saddle point and the presence of separate inner and outer transition states is less obvious.

The models we employ for the inner and the outer transition states are distinctly different. The outer transition state lies at large separations, beyond the van der Waals minimum, where only long-range interactions are important. Considerable effort has been devoted to the implementation of quantized versions of transition state theory^{72,73} for such long-range potentials to obtain accurate estimates for the low temperature limit rate. Here, we are more interested in somewhat higher temperatures (e.g., above about 10 K), with our primary focus on understanding where the transition from the long-range to the short-range transition state occurs, and what the effects of this transition are. In this temperature regime, classical transition state theory based approaches should be appropriate. Thus, we implement a particularly simple, yet classically accurate, version of variational transition state theory appropriate in the limit of large transition state separations.⁷⁴

The inner transition state is in the neighborhood of the saddle point on the potential energy surface. This saddle point arises as the chemical bond between the carbon and oxygen atoms begins to form, while the $\text{CC } \pi$ bond begins to break. The interplay between these two chemical forces determines the precise location of the saddle point, which turns out to be at about 2.2 Å separation between the C and O for the $\text{C}_2\text{H}_4 + \text{OH}$ reaction. At such short separations, the intermolecular forces

between the ethylene and hydroxyl moieties are quite strong. As a result, a simple rigid-rotor harmonic-oscillator treatment of all but the HOCC torsional mode, which will be treated as a one-dimensional (1D) hindered rotor, should provide a reasonably satisfactory treatment of the inner transition state. To illustrate this point we also present results for calculations involving the direct evaluation of a classical phase space based representation of the inner transition state partition function. The latter calculations provide a quantitative treatment of the full anharmonicities and couplings of the interfragment modes. Sophisticated *ab initio* methodologies are employed here in analyzing the energy of the saddle point and in obtaining appropriate vibrational frequencies and torsional potentials. For completeness, we also incorporate a variational reaction path treatment of this inner transition state region. However, for the temperatures of interest here, such variational effects are found to be minimal.

The computational methodologies employed for both the *ab initio* determinations, and for the kinetics evaluations are summarized in section II. Then, in section III, the quantum chemical results and the predictions for the rate constant are presented and discussed. This discussion focuses on a comparison with experiment and on the effect of the transition from a dominant outer to a dominant inner transition state as the temperature rises. Some concluding remarks are provided in section IV.

II. Computational Methodology

Ab Initio Calculations. The focus of the present *ab initio* quantum chemical calculations is on the accurate evaluation of the rovibrational properties of the reactants, the products, and the reaction path from the inner transition state inward. The highest-level geometry optimizations performed here involve restricted open-shell quadratic configuration interaction calculations with perturbative inclusion of the triples contribution⁷⁵ (roQCISD(T)), employing Dunning-style, triple- ζ basis sets (cc-pVTZ).⁷⁶ These optimizations are computationally intensive and so were restricted to C_s symmetry. The actual saddle point appears to have C₁ symmetry, as does the equilibrium geometry of the adduct.

Both unrestricted second-order Møller–Plesset perturbation theory (uMP2)^{77,78} and the unrestricted Becke–3 Lee–Yang–Parr (uB3LYP)⁷⁹ density functional were used to explore the reaction pathway in C₁ symmetry and to explore the vibrational properties. In particular, saddle points were located at both possible C_s symmetries and in C₁ symmetry with uMP2/cc-pVTZ calculations. Frequency calculations verified that the saddle point in C₁ symmetry was a first-order saddle point (i.e., one imaginary frequency) and the saddle points in C_s symmetry were second order (i.e., two imaginary frequencies). The intrinsic reaction coordinate was followed in both directions (again at the uMP2/cc-pVTZ level) to ensure that the transition states connect reactants (the C₂H₄...OH van der Waals adduct) to products (the C₂H₄OH molecular adduct). Projected vibrational frequencies were obtained along the pathway from the saddle points to the adduct at the same level of theory.

The saddle point vibrational frequencies were examined using molecular visualization to verify that the largest imaginary frequency corresponds to the reaction coordinate, while in C_s symmetry, the other imaginary frequency corresponds to a symmetry breaking motion that will be treated separately as a 1D hindered rotor. The C₁ symmetry saddle point was found to have a CCOH dihedral angle of 17°. The torsional potential in the neighborhood of this C₁ saddle point is extremely flat, with

the uMP2/cc-pVTZ energy difference between the C₁ and the lower of the C_s saddle points (CCOH dihedral angle of 0°) being less than 0.01 kcal/mol.

Higher-level saddle point frequency estimates were obtained at the unrestricted QCISD(T)/6-311G** level for a CCOH dihedral angle of 0°. The uQCISD(T)/6-311G** optimizations resulted in a saddle point of a geometry similar to that at the roQCISD(T)/cc-pVTZ level; e.g., at a CO bond length of 2.103 Å versus 2.136 Å. The frequency calculations again suggest that the C_s saddle point is of second order, with the largest imaginary frequency corresponding to the reaction coordinate and the additional imaginary frequency corresponding to the symmetry breaking motion of the CCOH torsion. uQCISD(T)/6-311G** geometry optimizations and frequency calculations for the infinitely separated products were also performed.

The zero-point energy change from reactants to the saddle point is substantially greater at the uMP2/cc-pVTZ level (2.43 kcal/mol) than at the uQCISD(T)/6-311G** level (1.67 kcal/mol). This result is not too surprising when one considers the large spin contamination ($\langle S^2 \rangle \approx 1.00$) in the wave function near the saddle point. Importantly, the QCISD(T) method is generally better able to handle the failures related to this spin contamination. Thus, the large difference strongly suggests some shortcoming in the uMP2/cc-pVTZ frequencies. Their implementation in transition state theory would result in inaccurate rate estimates, at least near room temperature and below, where a 0.8 kcal/mol energy difference correlates with a factor of 4 change in the rate. Notably, the two saddle point locations are quite similar, with the CO separation at the uMP2/cc-pVTZ level of 2.063 Å being only 0.040 Å shorter. Indeed, a reaction path projected frequency analyses suggests that the zero-point energy should change by only about 0.02 kcal/mol as a result of this difference in geometry. Furthermore, uMP2 evaluations with other basis sets indicate similarly increased zero-point differences, thereby indicating the inaccuracy is a fundamental flaw of second-order Møller–Plesset perturbation theory.

This apparent error in the uMP2 frequencies led us to also perform uB3LYP/6-311++G** frequency evaluations. The latter approach has only a minor spin contamination, with an $\langle S^2 \rangle \approx 0.77$ at a CO separation of 2.2 Å. Furthermore, B3LYP density functional theory generally provides much more consistent and accurate vibrational frequencies than does MP2. The absence of a saddle point introduces some ambiguity in the uB3LYP frequency evaluations. We have evaluated projected frequencies at the optimized geometries corresponding to constrained CO distances and also at the geometries obtained from an intrinsic reaction coordinate analysis starting at the optimized geometry for a CO separation of 2.2 Å. The latter geometry is chosen as the starting point for the intrinsic reaction coordinate analysis because it represents our best estimate of the transition state location, as discussed below. The former approach assumes that the CO separation provides a good representation of the reaction coordinate in the neighborhood of the saddle point. The two approaches yield essentially identical frequencies when correlated by their CO separations, yielding some confidence in either approach.

Table 1 provides a comparison of the frequencies and zero-point energy differences obtained with the uB3LYP/6-311++G**, uMP2/cc-pVTZ, and uQCISD(T)/6-311G** methods. The uB3LYP/6-311++G** results are seen to correlate very well with the uQCISD(T)/6-311G** ones, while the correlation with the uMP2/cc-pVTZ results is not nearly as good. This correlation between the uB3LYP and uQCISD(T) frequencies strongly suggests that both are reasonable and that the uMP2 estimates

TABLE 1: Vibrational Frequencies for the Stationary Points

species	method	vibrational frequencies ^a	ΔE_0^b
C ₂ H ₄ + OH	uQCISD(T)/6-311G(d,p)	822, 889, 948, 1038, 1229, 1365, 1474, 1663, 3134, 3152, 3216, 3242, 3765	
	uMP2/cc-pVTZ	827, 959, 983, 1076, 1246, 1384, 1485, 1685, 3180, 3198, 3269, 3295, 3824	
	uB3LYP/6-311++G**	835, 973, 976, 1058, 1238, 1377, 1471, 1683, 3122, 3137, 3194, 3223, 3709	
van der Waals minimum	uB3LYP/6-311++G**	74, 104, 105, 280, 363, 836, 986, 994, 1067, 1239, 1377, 1474, 1678, 3123, 3136, 3196, 3224, 3616	1.25
	uMP2/cc-pVTZ	76, 84, 115, 317, 354, 828, 975, 1000, 1082, 1248, 1383, 1487, 1678, 3180, 3196, 3269, 3295, 3752	
saddle point ($\tau = 0$)	uQCISD(T)/6-311G(d,p)	407i, 169i, 211, 367, 726, 822, 830, 953, 998, 1234, 1314, 1475, 1598, 3142, 3170, 3234, 3268, 3763	1.67
	uMP2/cc-pVTZ	514i, 55i, 229, 410, 748, 841, 1005, 1069, 1128, 1264, 1388, 1496, 1685, 3201, 3226, 3296, 3329, 3800	
	uB3LYP/6-311++G**	—, 82i, 190, 344, 642, 835, 919, 989, 995, 1239, 1333, 1474, 1585, 3132, 3161, 3217, 3257, 3746	
saddle point (C_1)	uMP2/cc-pVTZ	515i, 76, 231, 410, 749, 841, 1007, 1071, 1130, 1264, 1389, 1496, 1688, 3201, 3225, 3296, 3328, 3801	2.56
	uB3LYP/6-311++G**	—, 105, 213, 348, 645, 832, 923, 973, 994, 1236, 1336, 1472, 1607, 3136, 3160, 3221, 3254, 3752	
saddle point ($\tau = 180^\circ$)	uMP2/cc-pVTZ	626i, 188i, 196, 349, 765, 848, 996, 1037, 1104, 1271, 1368, 1495, 1654, 3205, 3213, 3298, 3324, 3802	2.16
	uB3LYP/6-311++G**	—, 199i, 164, 289, 644, 839, 894, 963, 985, 1244, 1331, 1460, 1570, 3136, 3143, 3222, 3249, 3736	
C ₂ H ₄ OH (C_1)	uB3LYP/6-311++G**	186, 345, 427, 560, 825, 949, 1077, 1119, 1178, 1354, 1395, 1452, 1483, 2975, 2995, 3136, 3245, 3818	3.60
C ₂ H ₄ OH ($\tau=0$)	uB3LYP/6-311++G**	301i, 76, 389, 598, 803, 931, 1051, 1164, 1217, 1278, 1401, 1466, 1521, 3026, 3059, 3132, 3237, 3825	3.11
C ₂ H ₄ OH ($\tau=180^\circ$)	uB3LYP/6-311++G**	129, 254, 416, 484, 858, 951, 1067, 1101, 1214, 1267, 1414, 1456, 1488, 2887, 2954, 3150, 3263, 3843	2.96

^a Vibrational frequencies in cm⁻¹. For uB3LYP saddle points the values are projected frequencies at $R = 2.2$ Å because there is no saddle point.

^b Change in zero-point energies from reactants to stationary point in kcal/mol.

are flawed. Thus, the uB3LYP/6-311++G** density functional should provide a computationally tractable, and yet accurate, approach for studying the projected frequencies along the reaction path in both C_s and C_1 symmetry. This approach was used in the final kinetics estimates for the inner transition state.

Final energy estimates for the saddle point, reactants, products, reaction path geometries, and van der Waals intermediate were obtained by computing single point energies using roQCISD(T) calculations with the Dunning-style, triple- ζ , and quadruple- ζ (cc-pVQZ) basis sets. These calculations were performed for the roQCISD(T)/cc-pVTZ C_s saddle point and reactant geometries and for all stationary points with the uB3LYP/6-311++G** geometries. Higher-level energies (E_{HL}) were estimated from an extrapolation to the infinite basis set limit via the expression^{80,81}

$$E(\infty) = E(l_{\text{max}}) - B/(l_{\text{max}} + 1)^4 \quad (4)$$

where l_{max} represents the maximum angular momentum in the basis set and B is a fitting parameter. The cc-pVTZ and cc-pVQZ basis sets correspond to $l_{\text{max}} = 3$ and 4, respectively. The higher-level energy is then calculated from the expression

$$E_{\text{HL}} = E[\text{QCISD(T)/cc-pVQZ}] + \{E[\text{QCISD(T)/cc-pVQZ}] - E[\text{QCISD(T)/cc-pVTZ}]\} \times 0.69377 \quad (5)$$

Alternative extrapolation schemes have been presented in the literature (see, e.g., ref 82 and its citations). Our experience with heats of formation for a large variety of C/O/H molecules and radicals suggests that the present formula is reasonably representative of any two-point formula and does yield near optimal agreement with experiment. Furthermore, since the extrapolation yields a correction of only 0.6 kcal/mol to the present saddle point energy, it is unlikely that any reasonable alternative

extrapolation scheme would yield more than a 0.1 kcal/mol change in this quantity.

Both the spin contamination ($\langle S^2 \rangle \approx 1.00$) in the unrestricted Hartree–Fock evaluations and the Q1 diagnostic⁸³ (~ 0.03) in the roQCISD(T) evaluations at the saddle point suggest that there is either significant multireference character or dynamic correlation to the wave function in that region. As a result, there is somewhat increased uncertainty about the accuracy of a QCISD(T) based energy estimate. For this reason, we have also estimated the saddle point energy relative to reactants with internally contracted multireference configuration interaction calculations with single and double excitations from a complete active space (CAS) self-consistent field (SCF) reference wave function. The roQCISD(T)/cc-pVTZ geometries were employed in these evaluations and the results for the cc-pVTZ and cc-pVQZ basis sets were extrapolated to the infinite basis set limit with an expression analogous to eq 5. Various active spaces were considered with the estimated saddle point energy generally decreasing somewhat with increasing number of active orbitals. The final calculations presented here are for a 7 electron 6 orbital CAS reference space consisting of the CC π and π^* orbitals (occupations of 1.91 and 0.09), the O radical (occupation of 1.00) and A'' lone pair orbitals (occupations of 2.00), and the OH σ and σ^* orbitals (occupations of 1.98 and 0.02); where the stated occupations are for a CO separation of 2.2 Å.

A referee has suggested that it may be interesting to compare our predictions with predictions from the CCSD(T) method. Our own experience is that, contrary to popular belief, the QCISD(T) method tends to provide better predictions than the CCSD(T) method. This is particularly notable when considering the dissociation of a molecule to form two doublet radicals, such as the dissociation of CH₄ to CH₃ + H. In this instance, both the QCISD(T) and CCSD(T) methods have an unphysical

turnover in their dissociation curves at large separations. However, the failure for the QCISD(T) method arises at a significantly larger separation (i.e., ~ 3.2 versus ~ 2.8 Å). Nevertheless, we have performed CCSD(T)/cc-pVTZ calculations and find that it predicts an increase in the saddle point energy relative to reactants of 0.3 kcal/mol over that obtained at the QCISD(T)/cc-pVTZ level.

The torsional potential in the saddle point region is extremely flat, particularly in the region from the C₁ minimum to the 0° CCOH dihedral angle, τ . Indeed, it is not completely clear whether the true torsional minimum at the saddle point is of C_s or of C₁ symmetry. The high-level calculations suggest the two energies differ by only 10 cm⁻¹. The uB3LYP/6-311++G** and uMP2/cc-pVTZ calculations predict very different CCOH dihedral angles of 50° and 17°, respectively.

The flatness of the potential between the minimum and $\tau = 0^\circ$, combined with the fairly significant torsional barrier at 180° (2.7 kcal/mol), implies that an accurate treatment of the contribution from the CCOH torsional motion to the transition state partition function requires a hindered rotor treatment based on a full torsional potential. Here, these potentials were based on five term cosine Fourier expansions designed to reproduce the three stationary point energies ($\tau = 0^\circ$, 50°, and 180°) and the vibrational frequencies at two of them ($\tau = 50^\circ$, and 180°). These Fourier expansions were obtained for each point along the uB3LYP/6-311++G** reaction path. The energies for the minima were obtained from higher-level calculations according to eq 5, while the frequencies were obtained from uB3LYP/6-311++G** evaluations. Sample calculations on a grid of torsional values indicate that the Fourier expansion provides a very good representation of the torsional potential.

At large separations there are effectively two degenerate electronic states corresponding asymptotically with the ²Π_{1/2} and ²Π_{3/2} states of OH. Within C_s symmetry these two states correlate with A' and A'' states, with the A' state correlating with the ground state of the C₂H₄OH adduct, while the A'' state correlates with a repulsive excited state. At the intermediate separations of the inner transition state, the extent of the separation between these two states is unclear. To explore the possible importance of the A'' state we have optimized the geometry at various constrained CO separations with the uB3LYP/6-311++G** method and then performed higher-level energy estimates according to eq 5.

The uB3LYP/6-31G* method was employed in the direct evaluation of the transitional mode contribution to the transition state partition function within the variable reaction coordinate formalism,⁸⁴ as discussed in more detail in the kinetics section. Corresponding reactant and saddle point vibrational analyses were also performed at the uB3LYP/6-31G* level to obtain reference rigid-rotor harmonic-oscillator based transition state theory results.

The quadrupole moment of ethylene and the dipole moment of OH are the key parameters in calculating the transition state partition functions for the outer transition state. Dipole moments of 1.68 and 1.69 D were evaluated with the uB3LYP/cc-pVQZ and uMP2/cc-pVQZ methods, respectively. These compare favorably with the experimental OH dipole moment of 1.66 D.⁸⁵ The same calculations yielded largest principle quadrupole moments⁷⁴ for C₂H₄ of 6.39 and 6.62 D Å, respectively; again agreeing well with the experimental value of 6.48 D Å.⁸⁶ The asymmetry in the quadrupole is very small, with the quadrupole moments for the other two axes being nearly identical.

All spin-restricted open-shell roQCISD(T) and multireference configuration interaction calculations were carried out using the

Molpro⁸⁷ quantum chemistry package. The remaining quantum chemical calculations were carried out using the Gaussian 98 suite of programs.⁸⁸

Kinetics. Transition state theory (TST) is now being widely used for the a priori calculation of rates.⁸⁹ The application of TST to the present reaction, and to other radical–molecule reactions, where the saddle point on the addition path lies lower in energy than reactants, is complicated by the presence of two separate transition states. At low temperatures, the dominant transition state lies at large separations (the outer transition state), while at higher temperatures, the dominant transition state lies in the neighborhood of the saddle point (the inner transition state).

At large separations, the longest-ranged term in the potential dominates and one may focus on just its effect on the kinetics. A recently described classical variational transition state theory treatment of the kinetics on long-range potentials is employed here.⁷⁴ For the addition of OH to C₂H₄, the dipole–quadrupole interaction provides the longest-ranged interaction. For that case, the capture rate on the long-range potential is predicted to be⁷⁴

$$k = C|dQ/\mu|^{1/2} \quad (6)$$

where d is the dipole moment of OH, Q is the largest principal quadrupole moment of C₂H₄, μ is the reduced mass for the C₂H₄, OH collision, and $C = 4.49$ when all quantities are expressed in atomic units. This expression yields a temperature independent rate coefficient of 3.6×10^{-10} cm³ molecule⁻¹ s⁻¹. Related expressions provided in ref 74 allow for the straightforward evaluation of the energy, E , and total angular momentum, J , resolved transition state number of states. Importantly, the E and J resolved transition state number of states is what is implemented in the evaluation of the rate coefficient according to eq 2.

The two key assumptions in this approach are (i) that the long-range potential provides an adequate description of the intermolecular interactions in the transition state region and (ii) that the moment of inertia for the centrifugal motion of the two fragments greatly exceeds the moments of inertia of the two fragments. The first approximation usually fails at a larger separation than the second one, with a separation of 10 bohr providing a reasonable first approximation to where it begins to fail significantly.⁹⁰ For the dipole quadrupole potential, the canonical transition state location R^\ddagger is given by

$$R^\ddagger = 0.91|dQ/T|^{1/4} \quad (7)$$

For C₂H₄ + OH this expression yields a transition state distance of 10 bohr at 71 K, implying that the long-range transition state treatment should be quite accurate below this temperature.

This temperature is somewhat lower than that at which the inner transition state becomes dominant (~ 130 K). However, it is more appropriate to consider the range of applicability at the microcanonical level. At the microcanonical level the transition state location is given by $1.17|dQ/E|^{1/4}$. For the present case, this implies that the transition state lies at a separation of 10 bohr at an energy of 0.39 kcal/mol. At the microcanonical level the inner and outer transition state numbers of states become equal at about 0.26 kcal/mol. Thus, the present long-range transition state treatment should be valid to beyond the crossing point of the two curves and thus should provide reasonable predictions for the current purposes. Furthermore, at even higher energies, the present treatment should still provide a semiquantitatively correct description of the flux at large separations.

Two quite different treatments of the inner transition state are considered here. The primary focus will be on a fairly standard approach based on direct summation over the rigid-rotor harmonic-oscillator (RRHO) energy levels. The parameters for these energy levels are determined from high-level quantum chemical calculations at a number of points along the reaction path⁹¹ as described above. For the CCOH torsional motion, a harmonic description is clearly of limited accuracy. Thus, a 1D classical phase space integral based treatment, which is again quite standard, is instead employed for this mode. A Pitzer–Gwinn approximation is applied to approximately correct for quantum effects.^{92,93} For completeness a 1D, Eckart-based tunneling treatment is incorporated for the reaction coordinate in the evaluation of the inner transition state number of states. In reality, however, this tunneling, which occurs from the van der Waals complex to the molecular complex, is expected to be of little importance in this reaction, because the saddle point on the potential energy surface lies below reactants.

In a number of prior studies of barrierless radical–radical reactions we have considered fully anharmonic treatments of all the interfragment modes via classical phase space integration.^{84,94} An important aspect of these prior analyses involved the consideration of multiple shapes (or reaction coordinates) for the transition state dividing surface. For the present radical–molecule case, the relatively short separation between the two reactants at the inner transition state (e.g., a CO separation of 2.2 Å at the saddle point) suggests that the simple harmonic-oscillator based description should be quite accurate. Nevertheless, it is interesting to study the extent of any anharmonic effects via the implementation of this variable reaction coordinate approach.

For the present application of the variable reaction coordinate (VRC) transition state theory (TST) approach, we employ the multifaceted-dividing-surface (MDS) formalism described in ref 95. With this approach, the dividing surface is defined by a fixed distance r between sets of pivot points on each of the fragments. For the OH fragment the pivot point is taken to be at the O atom. For the C₂H₄ fragment four symmetry-related pivot points are considered; with two pairs located a distance d above and below each C atom along a line perpendicular to the CC axis and passing through the C atom. For each different choice of d the distance r between the two pivot points is fixed so that the CO separation at the minimum energy point is effectively that of the high-level saddle point (i.e., 2.2 Å). d values ranging from 0 to 2 bohr are considered here. These MDS-TST evaluations are performed with the direct evaluation of the interaction potential at the uB3LYP/6-31G* level. To make a proper comparison with the related RRHO based analyses, we have also repeated the transition state vibrational analyses with the same uB3LYP/6-31G* method.

In prior VRC-TST applications, we have generally considered the fragment geometries to be constrained to those at infinite separation, thereby neglecting any effects due to structural rearrangement of the fragments as they react. At the 2.2 Å separation of the present inner saddle point, it is not clear that this rearrangement can be ignored. Indeed, the results presented below clearly indicate that the structural relaxation is a key aspect of the analysis. Thus, we have also considered a novel implementation of the VRC-TST approach in which the internal structures of each fragment for each configuration sampled in the direct evaluation of the transition state configurational integrals are optimized as part of the energy analysis.

This calculation of the geometry relaxation energy of the fragments employs a novel iterative process based on the normal

mode representation of the internal vibrational modes of the separated fragments. For a given overall configuration, at each step in the iteration, the Cartesian forces are evaluated analytically and transformed into internal fragment normal mode displacements using the normal modes of the fragments at infinite separation. These displacements were found to provide a reasonable description of the direction toward the potential energy minimum, but the distance to the minimum was generally overestimated. This deviation from the infinite separation quadratic model arises from both the change in the normal-mode frequencies and geometries, and the distortion of the potential energy from the quadratic form due to the interaction between the fragments. This distortion is taken into account by introducing a scaling factor for the normal mode displacements, which itself is calculated iteratively so that the energy is approximately minimized along the previously found direction in the normal modes coordinates space.

This procedure is followed to convergence with the required convergence varying with the interaction strength. For configurations with a negative interaction energy (relative to infinitely separated fragments), a high degree of convergence is requested (e.g., ~0.1 kcal/mol), while for points that are modestly repulsive a more modest convergence is requested. Highly repulsive geometries make little contribution to the transition state partition function, and no attempt is made to evaluate their relaxation energy. With this procedure, the direct evaluation of the relaxation energy only increased the computational time by about a factor of 2.

The two bottlenecks to the reactive flux are combined to provide an effective transition state number of states N_{eff}^\ddagger given by^{66,67}

$$\frac{1}{N_{\text{eff}}^\ddagger} = \frac{1}{N_{\text{inner}}^\ddagger} + \frac{1}{N_{\text{outer}}^\ddagger} - \frac{1}{N_{\text{max}}} \quad (8)$$

This expression assumes ergodicity between the inner and outer transition state, with statistical probabilities for crossing a given transition state. The quantities $N_{\text{inner}}^\ddagger$ and $N_{\text{outer}}^\ddagger$ are the number of available states at the inner and outer transition states, respectively, while N_{max} is the maximum flux between the two transition states. Although the van der Waals complex is not very deep (~1.7 kcal/mol), in a relative sense it is much lower than the saddle point. Furthermore, the vibrational frequencies in the van der Waals complex are much lower than those at the saddle point. Thus, it is reasonable to neglect the term in N_{max} , which reduces eq 8 to eq 2.

All of the present transition state theory evaluations are carried out at the energy, E , and total angular momentum, J , resolved level. The high-pressure limit capture rate is then obtained via eq 3. The experimental studies of the addition process have largely been performed at pressures of about 1 bar or lower. At such pressures, there may be some deviation of the rate coefficient from the high-pressure limit. Thus, we have also considered a 2D master equation analysis of the temperature- and pressure-dependent kinetics. This master equation analysis is based on the methodology described in ref 96. An exponential down model of energy transfer and Lennard-Jones collision rates are employed. The Lennard-Jones parameters for C₂H₄OH, He, and N₂ were taken to be $\sigma = 4.46, 3.68, \text{ and } 2.58 \text{ Å}$ and $\epsilon = 390, 92, \text{ and } 10 \text{ K}$, respectively.

One subtlety in the evaluation of eq 2 involves the treatment of the rovibronic states in the two, nearly degenerate, electronic states of OH (and thus of the interacting fragments) within the evaluation of $N_{\text{inner}}^\ddagger$ and $N_{\text{outer}}^\ddagger$. In the inner transition state

region the spin–orbit splitting is simply ignored, because it should be greatly reduced from its value at infinite separation. Furthermore, as illustrated below, the A'' state is high enough in energy at the inner transition state that it can be ignored and only one electronic state is considered. Thus, for the inner transition state, the sole effect of the spin–orbit interactions of the OH radical is assumed to involve an increase in the calculated interaction energy by 70 cm⁻¹, correlating with the spin–orbit lowering of the asymptotic OH ground electronic state, because this splitting is ignored in the present ab initio calculations. The present evaluation of $N_{\text{outer}}^{\ddagger}$ effectively involves an electronically decoupled classical evaluation of the OH rotational partition functions. Furthermore, we presume, because the fragments are only weakly interacting at large separations, that the spin–orbit splitting of the OH radicals is geometry independent. The overall $N_{\text{outer}}^{\ddagger}$ then includes one contribution from each spin–orbit state, with that from the second spin–orbit state shifted up by the spin–orbit splitting.

At low temperatures, the electronically decoupled classical evaluation of $N_{\text{outer}}^{\ddagger}$ necessitates an equivalent evaluation of the free OH rovibronic partition function for use in eq 3. However, at higher temperatures, where the inner transition state is the dominant bottleneck, it is best to employ the correct free OH rovibronic partition function obtained from a direct summation over the coupled quantized rovibronic energy levels. Here, we employ the decoupled classical evaluation of the free OH partition function as a reference and then incorporate an ad hoc correction factor to interpolate between the correct high- and low-temperature limits. This correction factor is taken to be $[k'_{\text{inner}}(T)k_{\text{outer}}(T)/(k'_{\text{inner}}(T) + k_{\text{outer}}(T))]/[k_{\text{inner}}(T)k_{\text{outer}}(T)/(k_{\text{inner}}(T) + k_{\text{outer}}(T))]$ where $k_{\text{inner}}(T)$ and $k_{\text{outer}}(T)$ are evaluated with the decoupled classical OH partition function and $k'_{\text{inner}}(T)$ is evaluated with the correct coupled quantum OH rovibronic partition function. This ad hoc correction factor is always less than unity and takes a minimum value of 0.78 at about 150 K. An improved treatment, involving for example, quantized rovibronic energy evaluations in the outer transition state region would not affect the conclusions reached below and was deemed beyond the scope of this work.

III. Results and Discussion

Potential Energy Surface. An illustrative plot of the lowest A', A, and A'' potential energy surfaces along the minimum energy path for various orientations is provided in Figure 1. The results plotted in Figure 1 are from HL//B3LYP/6-311++G(d,p)⁹⁷ calculations and do not include zero-point energy corrections. The maximum on the A surface for the optimal τ value arises at $R_{\text{CO}} = 2.2$ Å, and is at -1.74 kcal/mol relative to reactants. This A state correlates with the A' state in C_s symmetry. At this separation the A'' state is more than 10 kcal/mol higher in energy, clearly indicating the irrelevance of the A'' state to the flux through the inner transition state.

In the neighborhood of the saddle point the $\tau = 0$ and $\tau \approx 50^\circ$ potential values are nearly equivalent, while the $\tau = 180^\circ$ value is about 3 kcal/mol higher. A more detailed plot of the torsional dependence of the potential in the neighborhood of the saddle point is provided in Figure 2. The torsional potential gradually develops a sharper minimum near $\tau = 50^\circ$ as the CO separation decreases. At the equilibrium CH₂CH₂OH geometry the potential for the optimal torsional angle of 53.5° is 1.35 kcal/mol lower in energy than that for $\tau = 0$. In contrast, for the transition state separation, $R_{\text{CO}} = 2.2$ Å, it is not completely

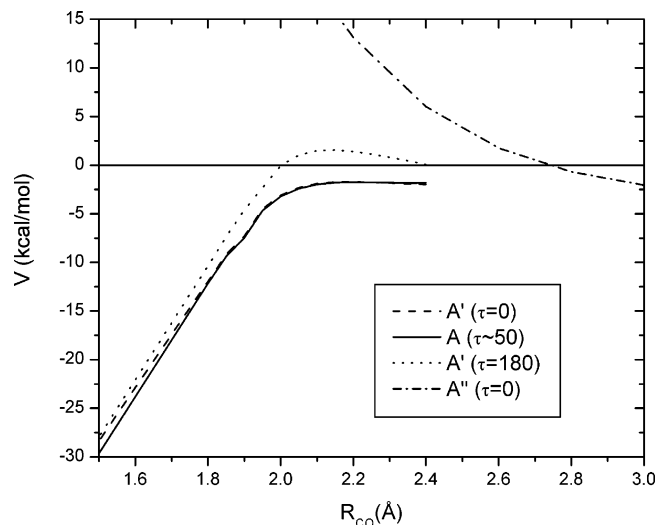


Figure 1. Plot of the minimum energy path potentials from HL//B3LYP calculations as a function of the constrained CO separation for the A' surface with $\tau = 0^\circ$ and 180° , for the A'' surface with $\tau = 0^\circ$, and for the ground state with an optimized τ value of $\sim 50^\circ$.

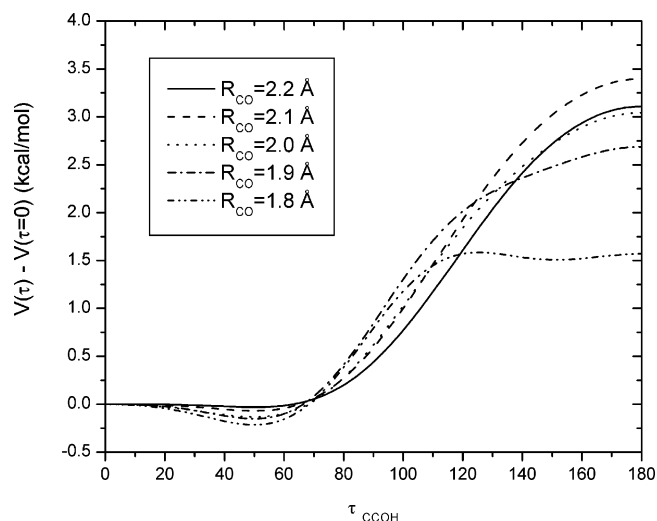


Figure 2. Plot of the HL//B3LYP CCOH torsional potential for a number of constrained CO separations.

clear whether the minimum is at 0 or at 50° . The extraordinarily flat behavior of the torsional potential from zero to 50° , coupled with the stronger dependence from 50° to 180° , strongly suggests that a harmonic treatment of this mode would be inadequate.

The present HL predictions for the zero-point corrected energies of the key stationary points are summarized in Table 2, along with the results of other high-level calculations from refs 61 and 57. Also included therein are the Q1 diagnostics for the QCISD(T)//B3LYP calculations. The geometries corresponding to these stationary points are illustrated schematically in Figure 3, with the corresponding Cartesian coordinates provided as Supporting Information.

The two HL predictions for the saddle point and C₂H₄OH energies in C_s symmetry are in good agreement. Notably, the HL//B3LYP prediction for the saddle point energy is higher for the C₁ geometry than for the $\tau = 0^\circ$ geometry. This result is primarily due to the inclusion of the zero-point energy for the torsional mode in the C₁ estimate but not in the $\tau = 0^\circ$ estimate, because the harmonic frequency for the latter is imaginary. The best estimate for the saddle point energy from the present calculations is -0.1 kcal/mol, which is obtained from

TABLE 2: Stationary Point Energies^a

species	B3LYP ^b	HL//B3LYP ^c	HL//QCISD(T) ^d	G2 ^e	BAC-G2 ^f	CBS-Q ^g	Q1 diag. ^h
van der Waals min.	-1.35	-1.70	-1.72	-2.07	-2.06	-1.94	0.010
saddle point (<i>C</i> ₁)	-3.52	-0.01		-1.23 <i>1.39</i>	-2.00	-2.90	0.026
saddle point ($\tau = 0$)	-3.61	-0.20	-0.38(-0.30) ⁱ				0.026
saddle point ($\tau = 180^\circ$)	-0.98	3.02					0.026
C ₂ H ₄ OH (<i>C</i> ₁)	-24.61	-26.98		-26.5 <i>-26.0</i>	-26.4	-26.9	0.012
C ₂ H ₄ OH ($\tau = 0$)	-23.44	-26.12	-26.15				0.012
C ₂ H ₄ OH ($\tau = 180^\circ$)	-22.88	-25.52					0.010

^a All energies in kcal/mol relative to C₂H₄ + OH including uB3LYP/6-311++G(d,p) zero-point corrections. ^b uB3LYP/6-311++G(d,p) energies. ^c Basis set extrapolated roQCISD(T) energies (cf. eq 5) evaluated at the uB3LYP/6-311++G(d,p) geometry. For the saddle point the *R*_{CO} = 2.2 Å constrained uB3LYP/6-311++G(d,p) optimized geometry is used, which corresponds to the maximum in the HL//B3LYP/6-311++G(d,p) minimum energy path potential. ^d Basis set extrapolated roQCISD(T) energies (cf. eq 5) evaluated at the roQCISD(T)/cc-pVTZ geometry. ^e G2 energies from refs 61 and 57, with the latter in italics. ^f BAC-G2 energies from ref 61. ^g CBS-Q energies from ref 61. ^h Q1 diagnostic for roQCISD(T)/cc-pvqz//B3LYP/6-311++G(d,p) calculation. For comparison the C₂H₄ and OH values are 0.011 and 0.009, respectively. ⁱ The number in parentheses denotes the maximum along the distinguished reaction path obtained from *R*_{CO} constrained optimizations with the roQCISD(T)/cc-pvtz method.

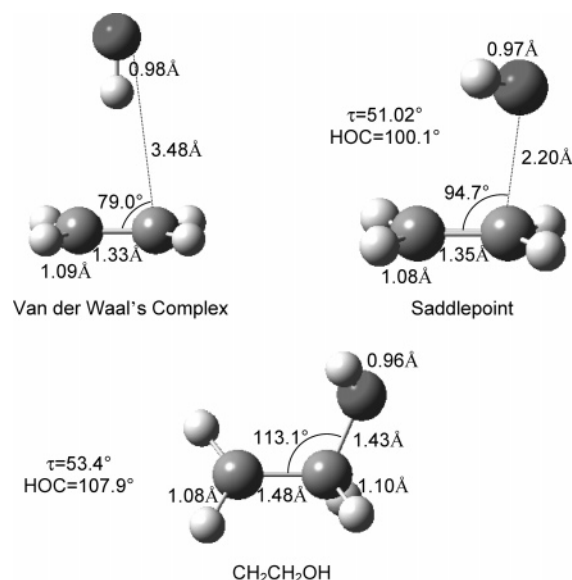


Figure 3. Illustration of the uB3LYP/6-311++G** optimized geometries for the van der Waals minimum, the optimized geometry for *C*₁ symmetry at *R*_{CO} = 2.2 Å, and for the C₂H₄OH molecular complex.

the HL//roQCISD(T) calculation for $\tau = 0^\circ$, added to the difference between the HL//B3LYP predictions for $\tau \approx 50^\circ$ and $\tau = 0^\circ$. This estimate also includes a spin-orbit lowering of the ground reactant state by 70 cm⁻¹ and a reduction in the saddle point energy by the harmonic zero-point energy for the torsional mode (52 cm⁻¹), because an anharmonic treatment would likely yield a frequency close to zero.

The G2, BAC-G2, and CBS-Q predictions from ref 61 yield lower saddle point energies, with the CBS-Q prediction being 2.8 kcal/mol lower. The variation in these estimates indicates a significant uncertainty in the estimated saddle point energy, as does the relatively large Q1 diagnostic of 0.03. For this reason we have also performed multireference configuration interaction (MRCI) calculations employing a 7-electron 6-orbital CAS reference wave function. These calculations employed roQCISD(T)/cc-pVTZ *R*_{CO} constrained geometries and were again extrapolated from cc-pVTZ and cc-pVQZ results to the infinite basis set limit. The $\tau = 0^\circ$ saddle point was again found to occur at *R*_{CO} = 2.2 Å, with an energy of 1.66 kcal/mol after inclusion of the uB3LYP/6-311++G(d,p) zero-point energy correction. This result includes the Davidson correction for higher-order excitations, while its neglect yields a saddle point energy of 3.64 kcal/mol. The difference between these two results is somewhat indicative of the uncertainty in the MRCI

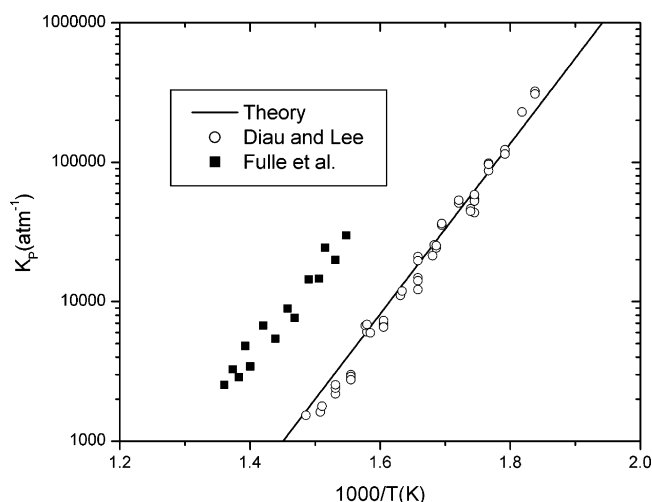


Figure 4. Plot of the predicted and experimentally observed temperature dependence of the equilibrium constant, *K*_p.

estimates. For the cc-pVQZ basis set the results are 1.98 and 3.84 kcal/mol, suggesting only a few tenths of a kcal/mol uncertainty from the basis set extrapolation. The relatively high value for the MRCI barrier height suggests that there is significant dynamic correlation in this system. Taken together, the MRCI, QCISD(T), and other high-level calculations suggest that the saddle point energy is -0.1 ± 2 kcal/mol.

The various high-level predictions for the energy of the C₂H₄-OH complex are in better agreement, differing by less than 1.0 kcal/mol. The experimental studies of Diau and Lee⁴⁹ and of Hippler and co-workers⁵¹ have yielded estimated reaction enthalpies of -30.2 ± 0.5 and -29.4 ± 1.4 kcal/mol, respectively. These values are considerably lower than the present 0 K estimate of -27.0 kcal/mol. However, the experimental values are for temperatures ranging from about 550 to 800 K. A direct comparison of the predicted and observed temperature-dependent equilibrium constants, as in Figure 4, provides a better indication of the accuracy of the theoretical predictions. The present predictions are seen to be in remarkable agreement with the experimental results of Diau and Lee,⁴⁹ while the order of magnitude discrepancy with the data of Hippler and co-workers⁵¹ suggests some shortcoming in that work.

Kinetics. The present predictions for the temperature dependence of the high-pressure C₂H₄ + OH addition rate are illustrated in Figure 5 for a variety of saddle point energies. For comparison the available experimental data for pressures of 600 Torr or higher, where the observed rate should be close

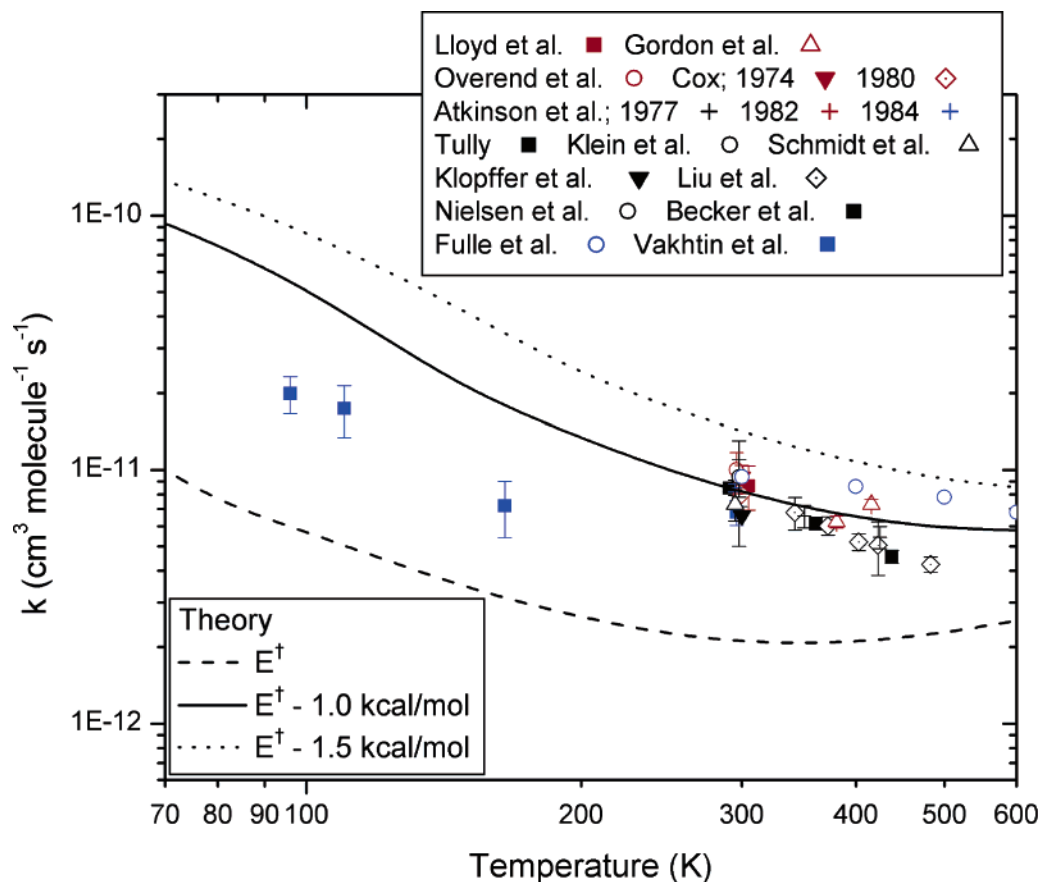


Figure 5. Plot of the temperature dependence of the high-pressure addition rate coefficient as predicted by the present effective transition state model for three different assumed inner saddle point energies. Also plotted are the available experimental rate coefficients determined for pressures of 1 bar or higher and the experimental data of Leone and co-workers⁵³ measured at lower temperatures and pressures.

to the high-pressure limit, are also plotted therein, as well as the low temperature (and low pressure) data of Leone and co-workers.⁵³ The predictions based on the current best estimate of -0.1 kcal/mol for the saddle point energy, given by the dashed line, are clearly lower than the experimental observations. Decreasing the ab initio predicted saddle point energy by 1.0 kcal/mol, to -1.1 kcal/mol, yields good agreement with the experimental data from 300 K on, while the reduction by 1.5 kcal/mol yields a rate that is somewhat too high. An adjustment by 1.0 kcal/mol is well within the bounds of the expected accuracy of the ab initio calculations, particularly in light of the large Q1 diagnostic for the QCISD(T) calculations in the neighborhood of the saddle point. Nevertheless, there are of course also significant uncertainties in the procedures for extracting kinetic estimates from the quantum chemical data. Thus, one should take the downward revision in the saddle point energy by 1.0 kcal/mol to be only suggestive of a likely error in the quantum chemical estimates. All further calculations presented here employ this adjusted barrier height. Note that we restrict our attention here to temperatures of 600 K or lower, because the abstraction reaction begins to interfere with measurements of the addition rate at that temperature.⁴⁴

Below room temperature the agreement between the adjusted predictions and Leone and co-workers⁵³ experimental observation appears to be unsatisfactory. However, these experiments are at quite low pressures (below 1 Torr), and thus, the discrepancy may simply be an indication of some falloff from the high-pressure limit. Leone and co-workers have argued that this should not be the case. Nevertheless, we have performed our own 2D master equation simulations of the pressure dependence. The results for a N₂ collider, employing a

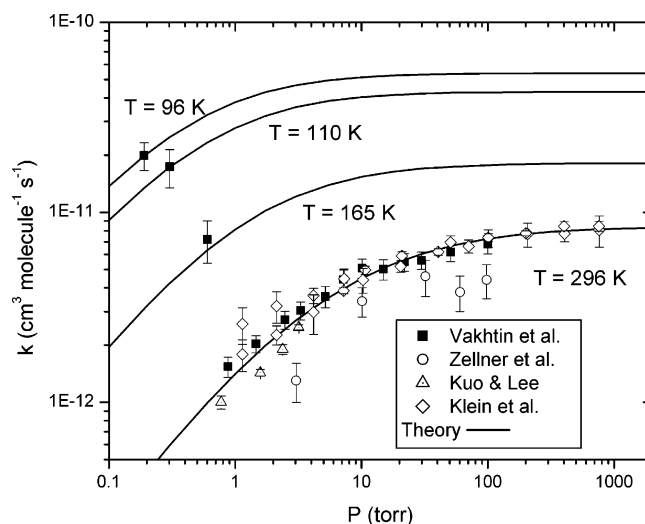


Figure 6. Plot of the predicted pressure dependence of the C₂H₄ + OH addition rate coefficient for N₂ as the bath gas at various temperatures. Also plotted are the corresponding experimentally observed rate coefficients for N₂, O₂, and air as the bath gases.

downward energy transfer parameter $\langle \Delta E_{\text{down}} \rangle$ of $200 (T/298)^{0.85}$ cm⁻¹, are illustrated in Figure 6 together with various experimental observations for N₂, Ar, and air (which are expected to behave quite similarly to N₂). The functional form for the energy transfer parameter was chosen on the basis of prior findings for similar systems.⁹⁸ The 298 K value of 200 cm⁻¹ is the value which best reproduces the data at 298 K, and again is completely reasonable in comparison with related studies. The agreement between theory and experiment is seen to be remarkably good.

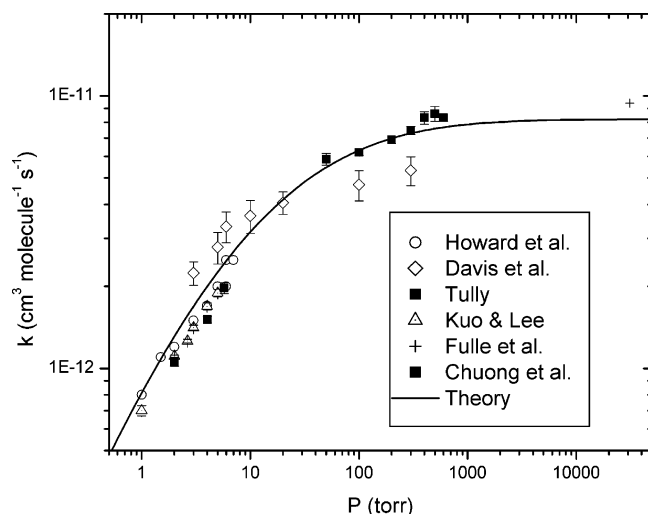


Figure 7. Plot of the predicted and observed pressure dependence of the $\text{C}_2\text{H}_4 + \text{OH}$ addition rate coefficient for He as the bath gas at room temperature.

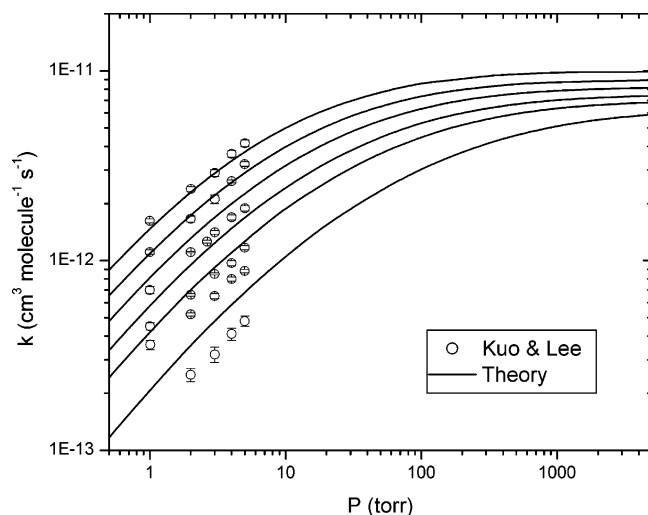


Figure 8. Plot of the predicted and observed pressure dependence of the $\text{C}_2\text{H}_4 + \text{OH}$ addition rate coefficient for He as the bath gas at temperatures of 251, 275, 300, 330, 360, and 430 K. The rate coefficients decrease with increasing temperature.

Related plots of the pressure dependence for the case of a He collider are shown in Figure 7 for results at ~ 300 K, and in Figure 8 for the results of Kuo and Lee for temperatures ranging from 251 to 430 K. In these simulations for a He collider we have chosen an equivalent functional form for the downward energy transfer parameter, but have set the 298 K value to be 100 cm^{-1} rather than 200 cm^{-1} . Again, this quite reasonable energy transfer parameter yields satisfactory agreement with experiment, particularly at 300 K, where the data is more extensive. The modest overpredictions ($\sim 30\%$) at higher temperatures in Figure 8 may be indicative of errors in the theoretical model (e.g., in the temperature dependence of either the energy transfer parameter or the high-pressure limit) or in the experimental data.

With this good agreement between theory and experiment for a wide range of temperatures and pressures, it is interesting to consider the relative contributions from the inner and outer transition states. The temperature dependence of these components are illustrated in Figure 9. The long-range transition state theory of ref 74, predicts a temperature-independent capture rate of $3.6 \times 10^{-10} \text{ cm}^3 \text{ molecule}^{-1} \text{ s}^{-1}$ for the present reaction. In contrast, the present negative saddle point energy corresponds

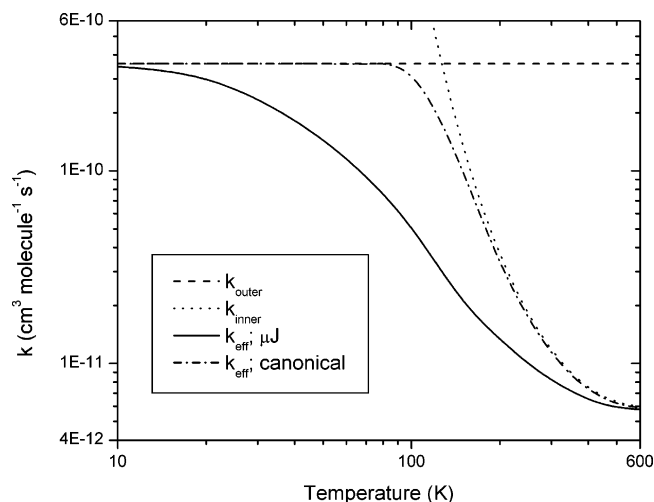


Figure 9. Plot of the temperature dependence of the high-pressure addition rate coefficient as predicted by the present effective transition state model, the inner transition state model, and the outer transition state model. For the effective transition state model, both E/J resolved evaluations (solid line; according to eq 2) and canonical evaluations (dashed–dotted line; according to eq 1) of the inner and outer transition state partition functions are illustrated.

to an inner transition state rate coefficient that is about $1 \times 10^{-11} \text{ cm}^3 \text{ molecule}^{-1} \text{ s}^{-1}$ near room temperature and then rapidly rises to infinity as the temperature decreases toward zero. The two rate coefficients cross at about 130 K. The E/J -resolved effective high-pressure addition rate coefficient (from eq 2) is significantly below (i.e., by more than 10%) each of the individual rate coefficients all the way from 10 to 400 K. At the crossing point of the inner and outer transition state predictions, the E/J -resolved effective rate coefficient is more than a factor of 10 lower. Notably, with canonical VTST evaluations of the transition state effective partition function (according to eq 1), this difference cannot exceed a factor of 2, as illustrated by the dashed–dotted line. At 300 K the E/J -resolved effective rate is still 30% lower than that from the inner transition state prediction. Clearly, the proper consideration of the two individual transition state regions at the E/J -resolved level is essential to the accurate modeling of the temperature dependence of this reaction.

The effect of neglecting the variational, the tunneling, or the 1D hindered rotor treatments of the inner transition state are illustrated in Figure 10. The variational considerations yield a reduction in the inner transition state rate coefficient by at most 15% with, as expected, the maximum reduction at the highest temperature considered of 600 K. The Eckart tunneling estimate provides a greater increase in the inner transition state rate coefficient, but only at lower temperatures, where the effect is ameliorated by the increasing dominance of the outer transition state bottleneck. The replacement of the hindered rotor treatment of the CCOH dihedral angle with a harmonic oscillator treatment has the greatest effect on the predicted capture rate.

A more global estimate of the effect of anharmonicities on the inner transition state predictions is provided by a comparison of phase space integral (PSI) based multifaceted-dividing-surface variable-reaction-coordinate TST predictions with the corresponding rigid-rotor harmonic-oscillator (including a 1D hindered rotor treatment) based TST results. The ratio of these two predictions is illustrated in Figure 11 for a variety of pivot point locations, d . In making this plot, we have included an approximate correction for quantum effects in the PSI-based results, because the vibrational frequencies for the transitional modes at the saddle point are large enough to have significant

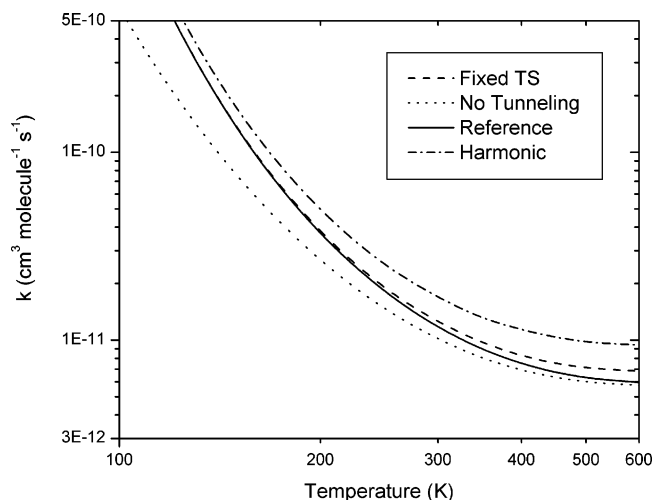


Figure 10. Plot of the predicted temperature dependence of the high-pressure addition rate coefficient for the inner transition state model, and ignoring tunneling, or anharmonicities in the torsional mode, or variational effects for the inner transition state.

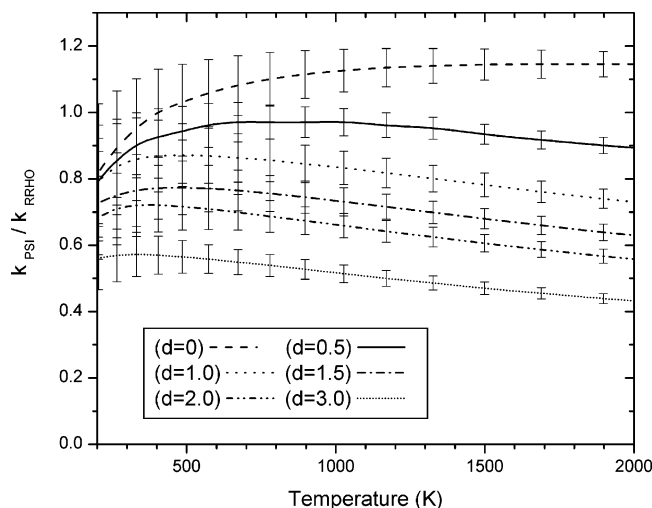


Figure 11. Plot of the ratio of the corrected multifaceted-dividing-surface variable-reaction-coordinate TST predicted high-pressure rate coefficient to that from the rigid rotor harmonic oscillator based inner transition state model.

quantum effects. In particular, the ratio of the quantum harmonic to classical harmonic canonical partition function for the transitional modes, which is illustrated in Figure 12, is applied as a correction factor to the PSI-based results, to make a proper comparison. The large deviation of this correction factor from unity, up to temperatures well beyond that at which the inner transition state becomes dominant, clearly indicates the importance of including quantum effects for these modes at lower temperatures. In contrast, for radical–radical reactions the vibrational frequencies for the transitional modes are considerably lower, and quantum effects can be safely neglected.⁹⁹

Another more modest correction factor involves the effect of the internal relaxation of the C₂H₄ and OH fragments in the neighborhood of the inner transition state. This effect can generally be neglected for radical–radical reactions, again due to the relatively large separations between the two fragments in that case. However, in the present radical–molecule reaction this effect is much larger, and thus, for the plot in Figure 11, we have corrected the PSI results by a Boltzmann factor in the uB3LYP/6-31G* relaxation energy at the saddle point. This correction assumes that the relaxation energy is independent of

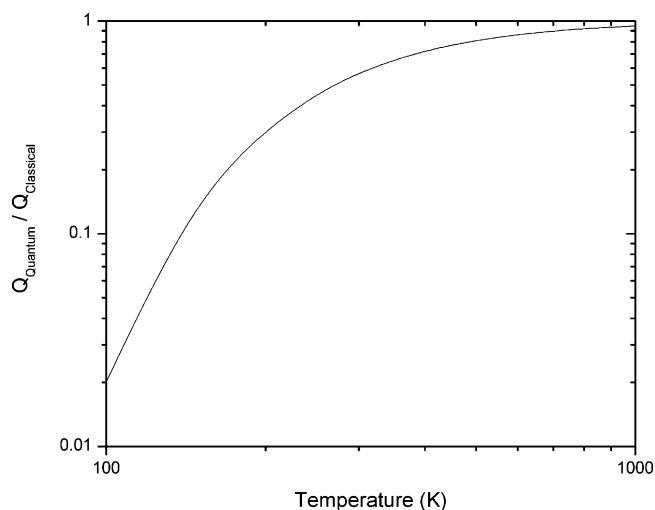


Figure 12. Plot of the ratio of the quantum harmonic to classical harmonic canonical partition function for the transitional modes as a function of temperature.

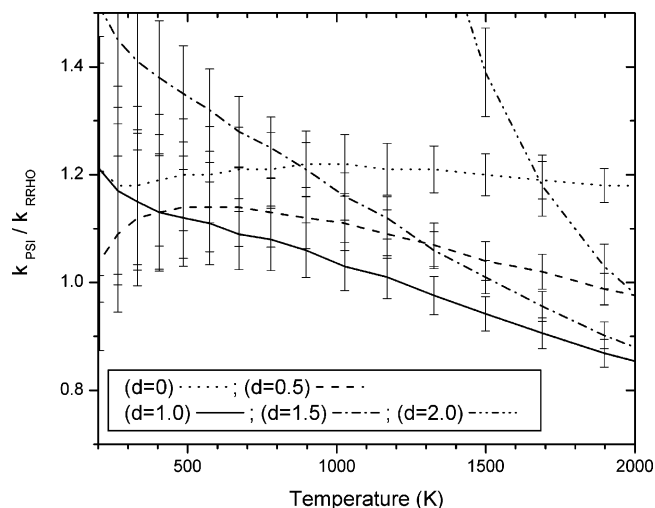


Figure 13. As in Figure 11, but including a direct calculation of the effect of geometry relaxation on the multifaceted-dividing-surface variable-reaction-coordinate predictions.

the relative orientation of the fragments within the inner transition state dividing surface.

With these corrections we see that the deviation of the ratio from unity, which is likely attributable to anharmonic effects, is quite small. However, there is one serious difficulty. In particular, the PSI-based predictions decrease monotonically with increasing pivot point distance d , and thus there is no variational minimum. If we had allowed d to continue to increase beyond 3 bohr, the PSI-predicted rate would have gradually gone to zero. The problem lies in the approximation of an orientation independent fragment relaxation energy.

To study this effect we have also performed a PSI-based analysis where the internal fragment structures are optimized for each orientation sampled in the configurational integral. The resulting predictions for the ratio of the PSI-based calculations to the RRHO-based calculations are illustrated in Figure 13. In this case, the ratio does go through a minimum at a pivot point of about $d = 1.0$ bohr, which corresponds to the typical pivot point location that we have observed in various related studies of radical–radical reactions. Now the effect of global anharmonicities and transitional mode couplings is predicted to be very small, with the ratio being about 1.0 ± 0.1 throughout the temperature range from 300 to 2000 K.

At this point it is perhaps worthwhile to return to a discussion of the activation energy defined as $-Rd(\ln k)/d(1/T)$. The predicted absence of significant anharmonic effects suggests that the present prediction for the inner saddle point energy of -1.1 kcal/mol should be quite reliable. Furthermore, this negative value for the saddle point does correlate, at least qualitatively, with the observed and predicted negative activation energy near room temperature. However, the slope of the plot of rate versus temperature near room temperature is quite different for the effective and inner transition state models, as seen in Figure 9. Indeed, the calculated room-temperature activation energies for the present effective and inner transition state models are -0.5 and -1.2 kcal/mol, respectively.

Activation energies similar to the present inner transition model were obtained in the studies of Villa et al.⁵⁶ (-0.92 kcal/mol) and of Vivier-Bunge and co-workers.⁵⁹ (-1.08 kcal/mol). Again, these activation energies were obtained with canonical transition theory state models that do not consider the effects of the outer transition state and thus do not provide reliable predictions, particularly for lower temperatures. Importantly, canonical implementations of transition state theory, in which the transition state partition function is optimized only as a function of T , are incapable of adequately describing the effect of the two transition states. The variational minimizations at the E, J -resolved level are a key component of the present model. For example, an effective transition state treatment implemented at the canonical level would yield a high-pressure rate coefficient of 1.8×10^{-10} cm³ molecule⁻¹ s⁻¹ at the crossing point between the inner and outer transition state model predictions (~ 130 K). This rate coefficient is about a factor of 6 greater than that obtained from the E, J -resolved effective transition state model. In the case of Vivier-Bunge and co-workers⁵⁹ the contribution from the temperature dependence of the partition functions has also been ignored.

IV. Conclusions

We have examined the low to moderate temperature addition of the hydroxyl radical to ethylene in the high-pressure limit and as a function of pressure, via high-level quantum chemical calculations, sophisticated VTST evaluations, and 2D master equation simulations. By simply reducing the inner saddle point energy by 1.0 kcal/mol from its ab initio predicted value (to -1.1 kcal/mol) we are able to satisfactorily reproduce the available experimental data from 100 to 600 K. The pressure dependence of the addition rate coefficient is also satisfactorily reproduced with reasonable parameters for the energy transfer function. The theoretically predicted capture rate is reproduced to within 10% by the expression $[4.93 \times 10^{-12}(T/298)^{-2.488} \exp(-107.9/RT) + 3.33 \times 10^{-12}(T/298)^{0.451} \exp(117.6/RT)]$; with $R = 1.987$ and T in K] cm³ molecules⁻¹ s⁻¹ over the 10 – 600 K range.

The use of an effective transition state model, incorporating effects from both the inner and outer transition states, is an essential element of the present predictions. It is particularly important that these effects be included at the energy, E , and total angular momentum, J , resolved level. At the point where the two transition states are of equal importance, the E/J resolved treatment yields a reduction in the rate by an order of magnitude. The long-range transition state theory of ref 74 provides a useful procedure for treating the outer transition state, while more standard rigid-rotor harmonic-oscillator plus 1D torsional treatments provide an appropriate model for the inner transition state. Other anharmonic effects appear to be minimal, at least for the present reaction.

The present calculations clearly show that a single transition state model is only appropriate for temperatures of about 400 K or higher. The convergence of the inner transition state model to the effective transition state model occurs at a temperature that roughly corresponds to the energy of the saddle point below reactants. This finding is likely quite general and can be used to estimate whether a single inner transition state treatment is sufficient for other reactions with negative saddle point energies.

The present model indicates that, for the $C_2H_4 + OH$ system at low temperatures, the decrease in the capture rate coefficient with increasing temperature is due to the increasing importance of the inner transition state. This finding likely provides an explanation for some related observations of the temperature dependence of radical–molecule reactions. For example, in the reaction of butenes with OH, where rates have been measured down to 23 K,¹⁰⁰ the experimental observations are remarkably analogous to those illustrated in the present Figure 9.

Acknowledgment. E.E.G. and S.W.N. gratefully acknowledge the support of the National Science Foundation (Grant No. CHE-0204705), the Environmental Protection Agency (Grant No. R03-0132), and the Texas Advanced Research Program (Grant No. 010366-0306). E.E.G. and S.W.N. also acknowledge the Combustion Research Facility at Sandia for visits to the CRF, the Laboratory for Molecular Simulation, Texas A&M Supercomputing Facilities and Dr. Charles Edwin Webster and Dr. Lisa M. Pérez for helpful discussions. The work at Sandia is supported by the Division of Chemical Sciences, Geosciences, and Biosciences, the Office of Basic Energy Sciences, the U.S. Department of Energy. Sandia is a multiprogram laboratory operated by Sandia Corporation, a Lockheed Martin Company, for the National Nuclear Security Administration under contract DE-AC04-94-AL85000.

Supporting Information Available: The Cartesian coordinates of the key stationary points obtained at the B3LYP/6-311++G(d, p) level. This material is available free of charge via the Internet at <http://pubs.acs.org>.

References and Notes

- Bedjanian, Y.; Laverdet, G.; Le Bras, G. *J. Phys. Chem. A* **1998**, *102*, 953.
- Farrell, J. T.; Taatjes, C. A. *J. Phys. Chem. A* **1998**, *102*, 4846.
- Knyazev, V. D.; Kalinovski, I. J.; Slagle, I. R. *J. Phys. Chem. A* **1999**, *103*, 3216.
- Timerghazin, Q. K.; Ariya, P. A. *Phys. Chem. Chem. Phys.* **2001**, *3*, 3981.
- Singleton, D. L.; Furuyama, S.; Cvetanovic, R. J.; Irwin, R. S. *J. Chem. Phys.* **1975**, *63*, 1003.
- Davis, D. D.; Huie, R. E.; Herron, J. T. *J. Chem. Phys.* **1973**, *59*, 628.
- Gaffney, J. S.; Atkinson, R.; Pitts, J. N. *J. Am. Chem. Soc.* **1975**, *97*, 6481.
- Biehl, H.; Bittner, J.; Bohn, B.; Geers-Muller, R.; Stuhl, F. *Int. J. Chem. Kinet.* **1995**, *27*, 277.
- Weber, M.; Hake, A.; Stuhl, F. *Int. J. Chem. Kinet.* **1997**, *29*, 149.
- Atkinson, R. *Chem. Rev.* **1986**, *86*, 69.
- Russell, J. J.; Senkan, S. M.; Seetula, J. A.; Gutman, D. *J. Phys. Chem.* **1989**, *93*, 5184.
- Muller-Markgraf, W.; Rossi, M. J.; Golden, D. M. *J. Am. Chem. Soc.* **1989**, *111*, 956.
- Seetula, J. A.; Russell, J. J.; Gutman, D. *J. Am. Chem. Soc.* **1990**, *112*, 1347.
- Nicovich, J. M.; Van Dijk, C. A.; Kreutter, K. D.; Wine, P. H. *J. Phys. Chem.* **1991**, *95*, 9890.
- Seakins, P. W.; Pilling, M. J.; Niiranen, J. T.; Gutman, D.; Krasnaperow, L. N. *J. Phys. Chem.* **1992**, *96*, 9847.
- Benson, S. W.; Dobis, O. *J. Phys. Chem. A* **1998**, *102*, 5175.
- Greiner, N. R. *J. Chem. Phys.* **1970**, *53*, 1284.

- (18) Morris, E. D.; Stedman, D. H.; Niki, H. *J. Am. Chem. Soc.* **1971**, 93, 3570.
- (19) Smith, I. W. M.; Zellner, R. *J. Chem. Soc., Faraday Trans. 2* **1973**, 69, 1617.
- (20) Bradley, J. N.; Hack, W.; Hoyeremann, K.; Wagner, H. G. *J. Chem. Soc., Trans. 1* **1973**, 69, 1889.
- (21) Stuhl, F. *Ber. Bunsen-Ges. Phys. Chem.* **1973**, 77, 674.
- (22) Cox, R. A. *Proc. Symp. Chem. Kinet. Data Upper Lower Atmos.* **1974**, 379.
- (23) Gordon, S.; Mulac, W. A. *Proc. Symp. Chem. Kinet. Data Upper Lower Atmos.* **1974**, 289.
- (24) Davis, D. D.; Fischer, S.; Schiff, R.; Watson, R. T.; Bollinger, W. *J. Chem. Phys.* **1975**, 63, 1707.
- (25) Atkinson, R.; Pitts, J. N., Jr. *J. Chem. Phys.* **1975**, 63, 3591.
- (26) Pastrana, A. V.; Carr, R. W. *J. Phys. Chem.* **1975**, 79, 765.
- (27) Howard, C. J. *J. Chem. Phys.* **1976**, 65, 4771.
- (28) Lloyd, A. C.; Darnall, K. R.; Winer, A. M.; Pitts, J. N., Jr. *J. Phys. Chem.* **1976**, 80, 789.
- (29) Bradley, J. N.; Capey, W. D.; Fair, R. W.; Pritchard, D. K. *Int. J. Chem. Kinet.* **1976**, 8, 549.
- (30) Overend, R.; Paraskevopoulos, G. *J. Chem. Phys.* **1977**, 67, 674.
- (31) Atkinson, R.; Perry, R. A.; Pitts, J. N., Jr. *J. Chem. Phys.* **1977**, 66, 1197.
- (32) Atkinson, R.; Perry, R. A.; Pitts, J. N., Jr. *J. Chem. Phys.* **1977**, 67, 3170.
- (33) Farquharson, G. K.; Smith, R. H. *Aust. J. Chem.* **1980**, 33, 1425.
- (34) Cox, R. A.; Derwent, R. G.; Williams, M. R. *Environ. Sci. Technol.* **1980**, 14, 57.
- (35) Atkinson, R.; Aschmann, S. M.; Winer, A. M.; Pitts, J. N. *Int. J. Chem. Kinet.* **1982**, 14, 507.
- (36) Tully, F. P. *Chem. Phys. Lett.* **1983**, 96, 148.
- (37) Klein, T.; Barnes, I.; Becker, K. H.; Fink, E. H.; Zabel, F. *J. Phys. Chem.* **1984**, 88, 5020.
- (38) Zellner, R.; Lorenz, K. *J. Phys. Chem.* **1984**, 88, 984.
- (39) Atkinson, R.; Aschmann, S. M. *Int. J. Chem. Kinet.* **1984**, 16, 1175.
- (40) Schmidt, V.; Zhu, G. Y.; Becker, K. H.; Fink, E. H. *Ber. Bunsen-Ges. Phys. Chem.* **1985**, 89, 321.
- (41) Klopffer, V. W.; Frank, R.; Kohl, E.-G.; Haag, F. *Chem.-Ztg.* **1986**, 110, 57.
- (42) Liu, A.-D.; Mulac, W. A.; Jonah, C. D. *Int. J. Chem. Kinet.* **1987**, 19, 25.
- (43) Liu, A.; Mulac, W. A.; Jonah, C. D. *J. Phys. Chem.* **1988**, 92, 3828.
- (44) Tully, F. P. *Chem. Phys. Lett.* **1988**, 143, 510.
- (45) Westbrook, C. K.; Thornton, M. M.; Pittz, W. J.; Malte, P. C. *Proc. Combust. Inst.* **1989**, 22, 863.
- (46) Nielsen, O. J.; Jorgensen, O.; Donlon, M.; Sidebottom, H. W.; O'Farrell, D. J.; Treacy, T. *Chem. Phys. Lett.* **1990**, 168, 319.
- (47) Becker, K. H.; Geiger, H.; Wiesen, P. *Chem. Phys. Lett.* **1991**, 184, 256.
- (48) Bott, J. F.; Cohen, N. *Int. J. Chem. Kinet.* **1991**, 23, 1075.
- (49) Diau, E. W.; Lee, Y.-P. *J. Chem. Phys.* **1991**, 96, 377.
- (50) Kuo, C.-H.; Lee, Y.-P. *J. Phys. Chem.* **1991**, 95, 1253.
- (51) Fulle, D.; Hamann, H. F.; Hippler, H.; Jansch, C. P. *Ber. Bunsen-Ges. Phys. Chem.* **1997**, 101, 1433.
- (52) Chuong, B.; Stevens, P. S. *J. Phys. Chem. A* **2000**, 104, 5230.
- (53) Vakhtin, A. B.; Murphy, J. E.; Leone, S. R.; *J. Phys. Chem. A* **2003**, 107, 10055.
- (54) Sosa, C.; Schlegel, H. B. *J. Am. Chem. Soc.* **1987**, 109, 4193.
- (55) Sosa, C.; Schlegel, H. B. *J. Am. Chem. Soc.* **1987**, 109, 7007.
- (56) Villa, J.; Gonzalez-Lafont, A.; Lluch, J. M.; Corchado, J. C.; Espinosa-Garcia, J. *J. Chem. Phys.* **1997**, 107, 7266.
- (57) Sekusak, S.; Liedl, K. R.; Sabljic, A. *J. Phys. Chem. A* **1998**, 102, 1583.
- (58) Yamada, T.; Bozzelli, J. W.; Lay, T. *J. Phys. Chem. A* **1999**, 103, 7646.
- (59) Alvarez-Idaboy, J. R.; Mora-Diez, N.; Vivier-Bunge, A. *J. Am. Chem. Soc.* **2000**, 122, 3715.
- (60) Hippler, H.; Viskolcz, B. *Phys. Chem. Chem. Phys.* **2000**, 2, 3591.
- (61) Pigeuras, M. C.; Crespo, R.; Nebot-Gil, I.; Tomas, F. *J. Mol. Struct.* **2001**, 537, 199.
- (62) Liu, G.-X.; Ding, Y.-H.; Li, Z.-S.; Fu, Q.; Huang, X.-R.; Sun, C.-C.; Tang, A.-C. *Phys. Chem. Chem. Phys.* **2002**, 4, 1021.
- (63) Singleton, D. L.; Cvetanovic, R. J. *J. Am. Chem. Soc.* **1976**, 98, 6812.
- (64) Johnston, H. S. *Gas Phase Reaction Rate Theory*; Ronald Press: New York, 1966.
- (65) Alternatively, one could include the van der Waals well in a multiple-well master equation analysis of the time-dependent populations. However, the very short lifetime of the van der Waals complex suggests that the limiting assumption of a collision-free environment should be completely satisfactory for all but extraordinarily high pressures.
- (66) Hirschfelder, J. O.; Wigner, E. *J. Chem. Phys.* **1939**, 7, 616. Miller, W. H. *J. Chem. Phys.* **1976**, 65, 2216. Chesnavich, W. J.; Bass, L.; Su, T.; Bowers, M. T. *J. Chem. Phys.* **1981**, 74, 2228. Rai, S. N.; Truhlar, D. G. *J. Chem. Phys.* **1983**, 79, 6046.
- (67) Klippenstein, S. J.; Khundkar, L. R.; Zewail, A. H.; Marcus, R. A. *J. Chem. Phys.* **1988**, 89, 4761.
- (68) Mozurkewich, M.; Benson, S. W. *J. Phys. Chem.* **1984**, 88, 6429. Mozurkewich, M.; Lamb, J. J.; Benson, S. W. *J. Phys. Chem.* **1984**, 88, 6435. Lamb, J. J.; Mozurkewich, M.; Benson, S. W. *J. Phys. Chem.* **1984**, 88, 6441.
- (69) Chen, Y.; Rauk, A.; Tschuikow-Roux, E. *J. Phys. Chem.* **1991**, 95, 9900. Chen, Y.; Tschuikow-Roux, J. *J. Phys. Chem.* **1993**, 97, 3742.
- (70) Jodkowski, J. T.; Rayez, M.-T.; Rayez, J.-C.; Berces, T.; Dobe, S. *J. Phys. Chem. A* **1998**, 102, 9219. Jodkowski, J. T.; Rayez, M.-T.; Rayez, J.-C.; Berces, T.; Dobe, S. *J. Phys. Chem. A* **1998**, 102, 9230.
- (71) Klippenstein, S. J.; Marcus, R. A. *J. Chem. Phys.* **1989**, 91, 2280. Klippenstein, S. J.; Marcus, R. A. *J. Chem. Phys.* **1990**, 93, 2418. Klippenstein, S. J.; East, A. L. L.; Allen, W. D. *J. Chem. Phys.* **1996**, 105, 118. Klippenstein, S. J.; Allen, W. D. *Ber. Bunsen. Phys. Chem.* **1997**, 101, 423.
- (72) Clary, D. C. *Annu. Rev. Phys. Chem.* **1990**, 41, 61 and references therein.
- (73) Troe, J. *Adv. Chem. Phys.* **1997**, 101, 819 and references therein.
- (74) Georgievskii, Y.; Klippenstein, S. J. *J. Chem. Phys.* **2005**, 122, 194103.
- (75) Pople, J. A.; Head-Gordon, M.; Raghavachari, K. *J. Chem. Phys.* **1987**, 87, 5968.
- (76) Dunning, T. H. *J. Chem. Phys.* **1989**, 90, 1007.
- (77) Head-Gordon, M.; Pople, J. A.; Frisch, M. J. *Chem. Phys. Lett.* **1988**, 153, 503.
- (78) Moller, C.; Plesset, M. C. *Phys. Rev.* **1934**, 46, 618.
- (79) Becke, A. D. *J. Chem. Phys.* **1993**, 98, 5648.
- (80) Feller, D.; Dixon, D. A. *J. Chem. Phys.* **2001**, 115, 3484–3496.
- (81) Martin, J. M. L. *Chem. Phys. Lett.* **1996**, 259, 669.
- (82) Helgaker, T.; Klopper, W.; Koch, H.; Noga, J. *J. Chem. Phys.* **1997**, 106, 9639.
- (83) Lee, T. J.; Taylor, P. R. *Int. J. Quantum Chem. Symp.* **1989**, 23, 199. Lee, T. J.; Rendell, A. P.; Taylor, P. R. *J. Phys. Chem.* **1990**, 94, 5463.
- (84) Klippenstein, S. J. *J. Chem. Phys.* **1992**, 96, 367. Klippenstein, S. J. *J. Chem. Phys. Lett.* **1993**, 214, 418. Klippenstein, S. J. *J. Phys. Chem.* **1994**, 98, 11459.
- (85) Peterson, K. I.; Fraser, G. T.; Klemperer, W. *Can. J. Phys.* **1984**, 62, 1502.
- (86) Dagg, I. R.; Read, L. A. A.; Smith, W. *Can. J. Phys.* **1982**, 60, 1431.
- (87) MOLPRO, version 2002.1. A package of ab initio programs written by Werner, H.-J.; Knowles, P. J. with contributions from Amos, R. D.; Bernhardsson, A.; Berning, A.; Celani, P.; Cooper, D. L.; Deegan, M. J. O.; Dobbyn, A. J.; Eckert, F.; Hampel, C.; Hetzer, G.; Korona, T.; Lindh, R.; Lloyd, A. W.; McNicholas, S. J.; Manby, F. R.; Meyer, W.; Mura, M. E.; Nicklaa, A.; Palmieri, P.; Pitzer, R.; Rauhut, G.; Schütz, M.; Schumann, U.; Stoll, H.; Stone, A. J.; Tarroni, R.; Thorsteinsson, T.; Werner, H.-J.
- (88) Frisch, M. J.; Trucks, G. W.; Schlegel, H. B.; Scuseria, G. E.; Robb, M. A.; Cheeseman, J. R.; Zakrzewski, V. G.; Montgomery, J. A., Jr.; Stratmann, R. E.; Burant, J. C.; Dapprich, S.; Millam, J. M.; Daniels, A. D.; Kudin, K. N.; Strain, M. C.; Farkas, O.; Tomasi, J.; Barone, V.; Cossi, M.; Cammi, R.; Mennucci, B.; Pomelli, C.; Adamo, C.; Clifford, S.; Ochterski, J.; Petersson, G. A.; Ayala, P. Y.; Cui, Q.; Morokuma, K.; Salvador, P.; Dannenberg, J. J.; Malick, D. K.; Rabuck, A. D.; Raghavachari, K.; Foresman, J. B.; Cioslowski, J.; Ortiz, J. V.; Baboul, A. G.; Stefanov, B. B.; Liu, G. Liashenko, A.; Piskorz, P.; Komaromi, I.; Gomperts, R.; Martin, R. L.; Fox, D. J.; Keith, T.; Al-Laham, M. A.; Peng, C. Y.; Nanayakkara, A.; Challacombe, M.; Gill, P. M. W.; Johnson, B.; Chen, W.; Wong, M. W.; Andres, J. L.; Gonzalez, C.; Head-Gordon, M.; Replogle, E. S.; Pople, J. A. *Gaussian 98*, revision A.11; Gaussian, Inc.: Pittsburgh, PA, 2001.
- (89) Truhlar, D. G.; Garrett, B. C.; Klippenstein, S. J. *J. Phys. Chem.* **1996**, 100, 12771.
- (90) Sample calculations suggest that at this separation, additional terms in the potential, such as those due to dispersion interactions, will yield only a modest (<35%) increase in the long-range predictions for the rate coefficient.
- (91) Miller, W. H.; Handy, N. C.; Adams, J. E. *J. Chem. Phys.* **1980**, 72, 99.
- (92) Pitzer, K. S.; Gwinn, W. D. *J. Chem. Phys.* **1942**, 10, 428.
- (93) Miller, J. A.; Klippenstein, S. J.; Robertson, S. H. *J. Phys. Chem. A* **2000**, 104, 7525.
- (94) Klippenstein, S. J.; Harding, L. B. *Phys. Chem. Chem. Phys.* **1999**, 1, 989. Klippenstein, S. J.; Harding, L. B. *J. Phys. Chem. A* **1999**, 103, 9388. Klippenstein, S. J.; Harding, L. B. *Proc. Combust. Inst.* **2000**, 28, 1503.

- (95) Georgievskii, Y.; Klippenstein, S. J. *J. Phys. Chem. A* **2003**, *107*, 9776. Georgievskii, Y.; Klippenstein, S. J. *J. Chem. Phys.* **2003**, *118*, 5442.
- (96) Miller, J. A.; Klippenstein, S. J.; Raffy, C. *J. Phys. Chem. A* **2002**, *106*, 4904.
- (97) The notation HL//B3LYP/6-311++G(d,p) refers to using the high-level energy estimates from the extrapolation scheme shown in eq 5 at B3LYP/6-311++G(d, p) optimized geometries.

- (98) Miller, J. A.; Klippenstein, S. J.; Raffy, C. *J. Phys. Chem. A* **2002**, *106*, 4904. Miller, J. A.; Klippenstein, S. J. *J. Phys. Chem. A* **2003**, *107*, 2680.
- (99) Klippenstein, S. J.; Marcus, R. A. *J. Chem. Phys.* **1987**, *87*, 3410; Yu, J.; Klippenstein, S. J. *J. Phys. Chem.* **1991**, *95*, 9882.
- (100) Sims, I. R.; Smith, I. W. M.; Bocherel, P.; Defrane, A.; Travers, D.; Rowe, B. R. *J. Chem. Soc., Faraday Trans.* **1994**, *90*, 1473.